analytical chemistry

pubs.acs.org/ac Article

Photoacoustic Heterodyne CO Sensor for Rapid Detection of CO Impurities in Hydrogen

Biao Li, Hongpeng Wu, Chaofan Feng, Jinmei Wang, Suotang Jia, Peichao Zheng,* and Lei Dong*

Cite This: *Anal. Chem.* 2024, 96, 547−553 Read Online

ACCESS | Metrics & More | Article Recommendations

ABSTRACT: Hydrogen (H_2) fuel cells have been developed as an environmentally benign, low-carbon, and efficient energy option in the current period of promoting low-carbon activities, which offer a compelling means to reduce carbon emissions. However, the presence of carbon monoxide (CO) impurities in H_2 may potentially damage the fuel cell's anode. As a result, monitoring of the CO levels in fuel cells has become a significant area of research. In this paper, a novel photoacoustic sensor is developed based on photoacoustic heterodyne technology. The sensor combines a 4.61 μm mid-infrared quantum cascade laser with a low-noise differential photoacoustic cell. This combination enables fast, real-time online detection of CO impurity concentrations in H_2. Notably, the sensor requires no wavelength locking to monitor CO online in real-time and produces a single effective signal with a period of only 15 ms. Furthermore, the sensor's performance was thoroughly evaluated in terms of detection sensitivity, linearity, and long-term stability. The minimum detection limit of 11 ppb was obtained at an optimal time constant of 1 s.

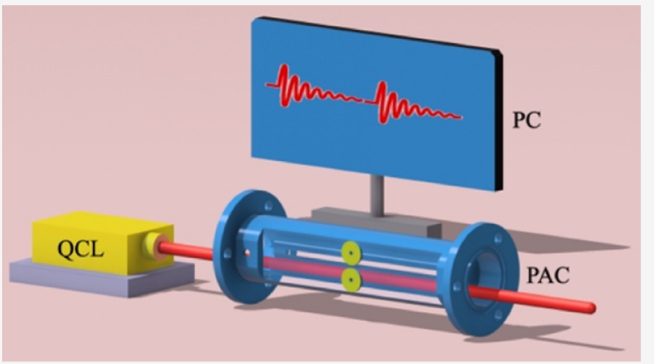

Fuel cells, in particular hydrogen (H_2) fuel cells, have drawn a lot of interest as cost-effective and highly effective energy sources in a variety of applications.[1] While limiting their negative effects on the environment, these electrochemical devices efficiently transfer the chemical energy found in fuels like H_2 into electricity.[2−8] Therefore, fuel cells present an appealing way to reduce carbon emissions. However, the presence of contaminants in the H_2 fuel stream, such as carbon monoxide (CO), can dramatically reduce fuel cell performance, jeopardizing both efficiency and safety.[9] Consequently, detecting and monitoring CO in fuel cells have become a key focus area, driven by the necessity for clean and pure H_2 fuel.

Hydrogen is typically produced through a variety of processes, including the reforming of natural gas and the gasification of biomass.[10] Trace quantities of CO develop accidentally during these processes, possibly polluting H_2. Furthermore, CO in H_2 fuel may contaminate catalysts, particularly at the anode of fuel cells. The electrochemical reactions that take place during power generation are slowed by CO molecules adhering to the catalyst surface. This phenomenon reduces the amount of active surface area that is accessible for H_2 oxidation, which has a negative impact on the performance of fuel cells overall.[11,12] Reports indicate that subjecting a fuel cell to an environment with a CO concentration of 70 ppm (ppm) for 6 h can lead to an 85% loss in voltage, the CO content at the platinum anode should be kept below 10 ppm for platinum anodes and below 100 ppm for platinum−ruthenium anodes for the best fuel cell performance and lifespan.[13,14] Moreover, CO poisoning can inflict irreparable damage to the catalyst and other critical components, leading to a shortened lifespan for the fuel cell system. Consequently, the development of effective CO detection methods is crucial to maximizing the efficiency and reliability of fuel cell systems. This, in turn, contributes to the advancement of fuel cell technology and accelerates the transition to a clean and sustainable energy future.

A variety of methods have been developed for the detection of CO. These methods encompass electrochemical sensors, metal oxide sensors, catalytic combustion sensors, and others. However, these approaches have drawbacks that restrict their ability to detect CO in H_2. For instance, electrochemical sensors exhibit poor selectivity and are highly influenced by environmental factors.[15,16] Metal oxide sensors suffer from stability issues and necessitate regular calibration and maintenance.[17,18] Catalytic combustion sensors are susceptible to interference from other gases and have a limited

Received: October 22, 2023
Revised: December 18, 2023
Accepted: December 20, 2023
Published: December 29, 2023

https://doi.org/10.1021/acs.analchem.3c04753
Anal. Chem. 2024, 96, 547−553

lifespan.[19,20] Consequently, there exists an urgent need for the development of an exceptional sensor capable of monitoring the level of CO in H_2. Such a sensor should possess high sensitivity, high selectivity, fast response time, and good stability, require no calibration, and offer real-time monitoring capability.

In recent years, due to its many benefits, which include low background, no wavelength selectivity, a broad dynamic range, and proportionality to optical power, photoacoustic spectroscopy has recently attracted more and more interest.[20−39] The photoacoustic heterodyne technology based on photoacoustic cells (PAC) has emerged as a promising candidate for CO monitoring in H_2 among the numerous photoacoustic spectroscopy approaches. Such sensors combine the benefits of conventional photoacoustic spectroscopy, eliminate the need for frequency calibration and wavelength locking, and have a faster response time. In this work, a differential PAC-based photoacoustic heterodyne sensor for real-time CO in H_2 monitoring is presented. Compared to other photoacoustic spectroscopy sensors, this one provides a faster response time and a simpler optical setup and does away with the requirement for frequency calibration and wavelength locking.

EXPERIMENTS

Photoacoustic Heterodyne Sensor. Figure 1 presents a schematic diagram of the photoacoustic heterodyne sensor

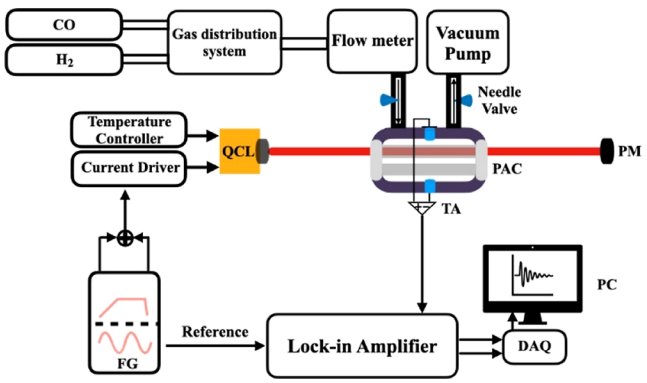

Figure 1. Schematic of the experimental setup. QCL: quantum cascade laser; PAC: photoacoustic cell; TA: trans-impedance amplifier; FG: function generator; DAQ: data acquisition card; PC: personal computer; PM: power meter.

utilized in this work. A DFB-QCL (AdTech Optics, model HHL-17−62) instrument with a center wavelength of 4.61 μm was employed as the excitation light source. To ensure the laser operated within the absorption line of CO, precise control of the laser was achieved using a current controller (ILX Lightwave, model LDX-3220) and a temperature controller (Thorlabs, model TED 200C). A dual-channel function generator (Tektronix, model AFG 3022) generated sine and trapezoidal scanning waveforms, serving as the modulation and scanning signals for the laser, respectively. The frequency of the sine wave was 6776 Hz, which was 273 Hz away from the resonance frequency of the PAC under H_2 carrier gas. The experiment utilized the 1f wavelength modulation technique to maximize the resulting beat frequency signal.[40,41] The laser current corresponding to the trapezoidal scanning waveform ranged from 198 to 234 mA. The rising edge of the trapezoidal scanning waveform lasted for 7 ms, with an overall duration of 15 ms. The function generator sent a synchronization signal to a lock-in amplifier (Stanford Research Systems, model SR830), which demodulated the electrical signals transmitted by the microphone to the lock-in amplifier. To enhance the signal-to-noise ratio of the sensor, a low-noise differential PAC was employed.[42] The PAC featured two high-transmittance (Ψ25.4 × mm) CaF_2 windows with a transmittance exceeding 95%. The PAC included an air inlet, an air outlet, and two high-sensitivity microphones (model EM258 from Primo Microphones, Japan) for detecting acoustic signals. The resulting acoustic signal was converted into an electrical signal, amplified by a preamplifier, and demodulated by a lock-in amplifier. The demodulated signal was then transmitted to a personal computer equipped with a data acquisition card for data recording and analysis. Needle valves were present at both ends of the gas line, allowing for the regulation of gas flow by adjusting the needle valve switches. A manometer (MKS Instrument, model 649B) and a flow meter (Alicat Scientific, model M-2 SLPM-D/5 M) provided real-time displays of the operating pressure and flow rate within the gas line. A vacuum pump (Oerlikon Leybold Vacuum Inc., model D16C) was employed to introduce the gas to be measured into the PAC. Different concentrations of CO required for the experiments were achieved using a gas distribution system (Environics, model EN4000), which varied the mixing ratio of 150 ppm of CO in H_2 to obtain the desired concentration.

Frequency and *Q*-Value of Differential PAC. In this work, the low-noise differential PAC utilized possesses a cavity length of 90 mm and an inner diameter of 8 mm. Notably, the experiment's use of H_2 as the carrier gas results in a change in the PAC's resonance frequency. In contrast to the case where N_2 serves as the carrier gas, the resonance frequency experiences an increase while the quality factor (Q-value) undergoes a decrease. This discrepancy stems from the differing adiabatic index and molar masses between H_2 and N_2 (H_2: adiabatic index of 1.41, molar mass of 0.002 kg/mol; N_2: adiabatic index of 1.4, molar mass of 0.028 kg/mol). Employing the theoretical formula $f = \frac{v}{2L}$ and $v = \sqrt{\frac{\kappa R_0 T}{\sum_1^n M_n C_n}}$, where L is the effective length of the resonator and v is the speed of sound, κ is an adiabatic index, R_0 is the molar gas constant, T is the temperature, n is the type of mixed gas, and M_n and C_n are the molar mass and the concentration of the n-th analyte in the mixture, respectively. The calculated resonance frequency of the PAC stands at 7219.9 Hz, with a Q-value of 35. During the experiment, the PAC was filled with 10 ppm of CO: H_2 gas mixture, and the frequency response curve was generated by modulating the frequency of the excitation light source, as shown in Figure 2. The resulting resonance frequency, with a Q-value of 31, is 7048.9 Hz. It is important to note that the reason for the discrepancy between the theoretically calculated value and the actual measured value is that the calculation process assumed the medium to be an ideal fluid, ignored the viscosity of the gas, and approximated the propagation of sound waves as an adiabatic process.

Measurement of Photoacoustic Heterodyne Signal. In the technique of photoacoustic heterodyne, efficient generation of photoacoustic heterodyne signals requires setting the modulation frequency of the excitation light source to a nonresonant frequency f of the PAC, which has a frequency difference Δf from f_0. The photoacoustic signals generated by the PAC are then demodulated by 1f at f. To determine the optimal modulation frequency, a 150 ppm of CO: H_2 gas

https://doi.org/10.1021/acs.analchem.3c04753
Anal. Chem. 2024, 96, 547−553

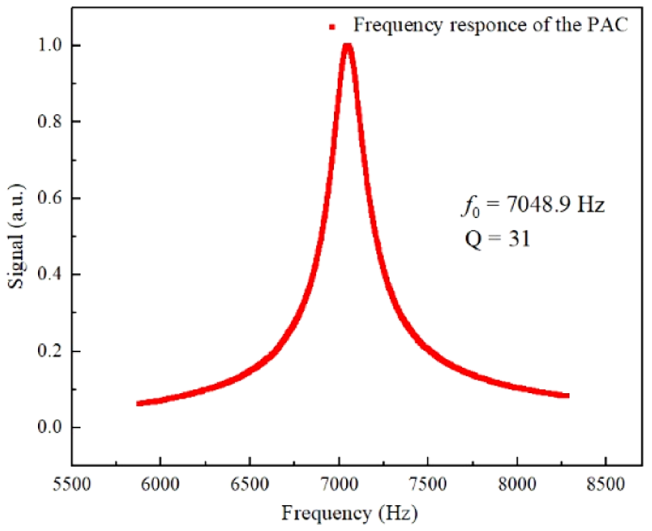

Figure 2. The frequency response curve of the PAC in an H_2 carrier gas.

mixture was introduced into the photoacoustic heterodyne sensor. The pressure and gas flow rate in the PAC was set to atmospheric pressure and 50 sccm, respectively. By variation of the modulation frequency, different peak photoacoustic heterodyne signals were obtained and are recorded in Figure 3. As shown in Figure 3, the optimal modulation frequency f is

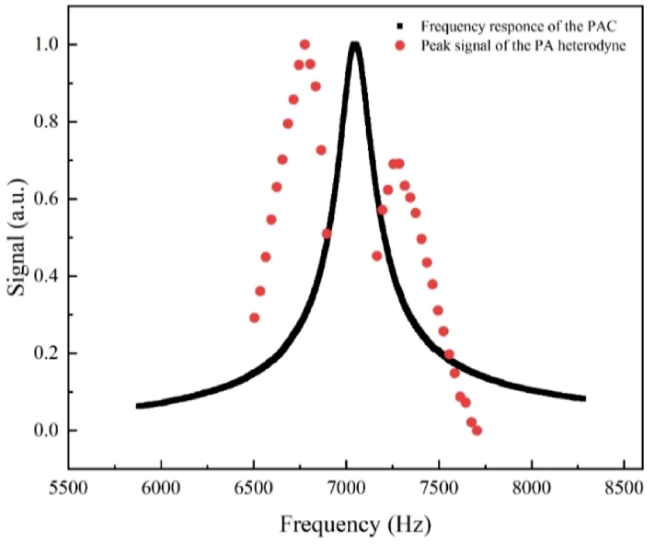

Figure 3. Amplitudes of the photoacoustic heterodyne signals and conventional PAS signals as a function of the modulation frequency.

6776 Hz, which is 273 Hz away from the resonance frequency f_0. It is noteworthy that the Δf value differs from the previously reported Δf = 114 Hz,[43] and this difference may be attributed to the smaller Q-value of the PAC. According to the formula of the photoacoustic heterodyne signal:[43] $s = \frac{1}{2}\xi_0 e^{-t/\tau}\cos[2\pi(f_0 - f)t - \varphi_0]$, where τ represents the damping time of the sound vibration corresponding to the Q-value of the PAC. The smaller the Q-value, the faster the damping time of the sound vibration, resulting in a shorter interval between the peaks and valleys of the photoacoustic heterodyne signal, and thus a shorter Δt value. Since $\Delta f = 1/\Delta t$, it causes Δf to be larger. Additionally, a faster speed of sound would further reduce the Δt. Moreover, the observed trend of signal variation with modulation frequency exhibits distinct asymmetry, deviating from the findings reported in this field previously. This discrepancy arises from the reduction in carrier gas density, resulting in an increased resonance frequency of the photoacoustic cell and a larger offset frequency. Consequently, in comparison to previous reports, the phenomenon wherein the photoacoustic signal is inversely proportional to the modulation frequency is notably magnified.

Figure 4 illustrates the photoacoustic heterodyne signal with a time interval of 15 ms for generating each photoacoustic

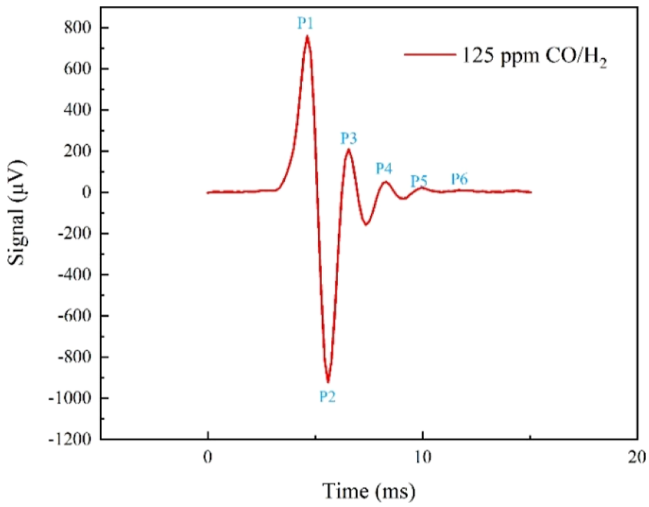

Figure 4. Measured photoacoustic heterodyne signal.

heterodyne signal. Utilizing the beat frequency algorithm,[40] the resonance frequency f_0 of the PAC, and the Q-value can be calculated. The figure exhibits six peaks, where the steady-state response dominates when the P1 peak is generated and the transient response of the PAC begins with the appearance of the P2 peak.

To fit the frequency and Q-value, an exponential decay function is applied to the five peaks, P1, P3, P4, P5, and P6. The time interval Δt between P3 and P1 is measured at 3.56 ms, with a decay time τ of 1.47 ms. Utilizing the beat frequency algorithm,[40,41,43] the resonant frequency of the PAC is determined to be f_0 = 7056 Hz, and the Q-value is calculated as Q = 32.5. In the measurement process, the insights derived from this fitting procedure can be utilized to provide feedback to the function generator through the LabVIEW program, enabling the implementation of a self-calibration process.

To calculate the amplitude of the photoacoustic heterodyne signals, the peak value of P3 is subtracted from the peak value of P2. For 125 ppm of CO: H_2 gas mixture, the maximum signal amplitude is measured at 1132.7 μV. The standard deviation 1σ of the background noise is determined to be 3.29 μV.

Scan Time and Lock-in Time Constant Optimization. The rate at which the excitation light wavelength can be adjusted by modifying the period of its scanning function. In this work, we examined the variation in the amplitude of the photoacoustic heterodyne signal output from the photoacoustic heterodyne sensor with respect to the scanning period of the excitation light wavelength. A 150 ppm of CO: H_2 gas mixture was introduced into the sensor, and the scanning period of the excitation light wavelength was altered

https://doi.org/10.1021/acs.analchem.3c04753
Anal. Chem. 2024, 96, 547−553

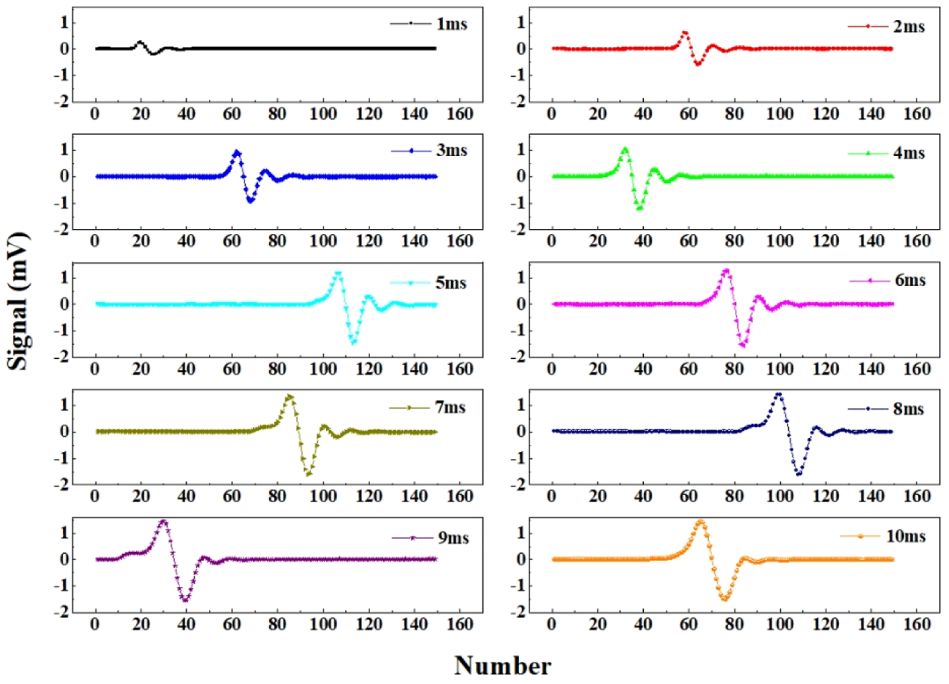

Figure 5. Photoacoustic heterodyne sensor output signals for different excitation wavelength scanning periods.

from 1 to 10 ms. The sensor responses were recorded and are depicted in Figure 5. The results indicate that as the scanning period of the excitation light wavelength increased, the amplitude of the sensor photoacoustic heterodyne signal exhibited a trend of initially increasing and then decreasing. Notably, the optimal response amplitude of the sensor was observed when the scanning period of the excitation light wavelength was set to 7 ms. Furthermore, with the increase in the scanning period of the excitation light wavelength, the response mode of the PAC gradually transitioned from the transient response mode to the steady-state response mode. This transition is clearly observed in Figure 5, particularly in the case of the 10 ms scanning period. In this case, the output signal from the sensor nearly transformed into a harmonic signal, signifying the dominance of the steady-state response mode.

The sensor response time becomes faster as the time constant of the lock-in amplifier decreases. This characteristic is particularly crucial for rapid measurements. Hence, the time constant of the lock-in amplifier in the sensor is fine-tuned for optimization. In the experiment, 150 ppm of CO: H_2 gas mixture was introduced into the sensor, and the time constant of the lock-in amplifier was varied to observe the resulting sensor response signal, as depicted in Figure 6. The findings reveal that the optimal time constant is 1 ms. It is worth noting that while smaller time constants yield stronger signals, they also introduce higher levels of noise. This trade-off is illustrated in Figure 7, which displays the signal-to-noise ratio as a function of the time constant. The signal-to-noise ratio of the photoacoustic heterodyne signal output by the sensor exhibits a continuous increase as the time constant extends from 30 μs to 1 ms. Subsequently, with a further increase in the time constant, the system's signal-to-noise ratio declines. This is primarily attributed to the system introducing excessive background noise due to an overly broad detection bandwidth at this point. When the time constant of the lock-in amplifier is

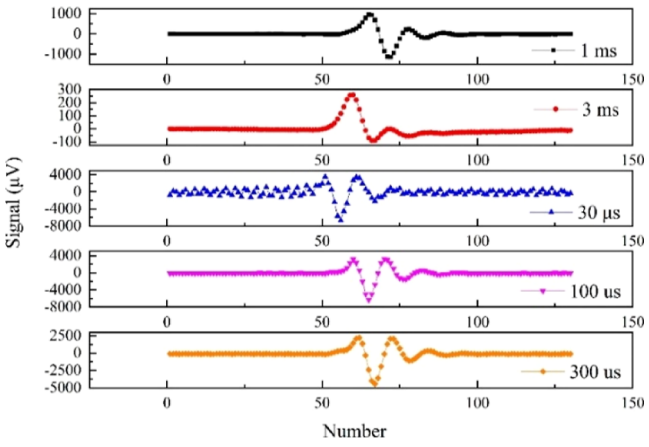

Figure 6. Response of the photoacoustic heterodyne sensor in the case of different time constants of the lock-in amplifier.

set to 1 ms, the signal-to-noise ratio of the sensor is measured to be 420.7.

Photoacoustic Heterodyne Sensor Linearity and Stability. The linearity of the photoacoustic heterodyne sensor was assessed under atmospheric pressure and a gas flow rate of 50 sccm. The CO: H_2 mixtures with different concentration levels of 0, 50, 75, 100, 125, and 150 ppm were directed into the sensor in turn. At each concentration level, two hundred data points were recorded, and the results are depicted in Figure 8a. For the 50 ppm of CO concentration, the amplitude of the photoacoustic detector signal was measured to be 454 μV, with a background noise level (1σ) of 3.3 μV, resulting in a signal-to-noise ratio of 137.6. The detection sensitivity was determined to be 363 ppb, and the normalized noise equivalent absorption coefficient (NNEA) was calculated to be 3.76×10^{-8} cm^{-1} W Hz$^{-1/2}$. Moreover, Figure 8b displays the average signal amplitudes at different concentration levels, with a high R-squared value of

https://doi.org/10.1021/acs.analchem.3c04753
Anal. Chem. 2024, 96, 547−553

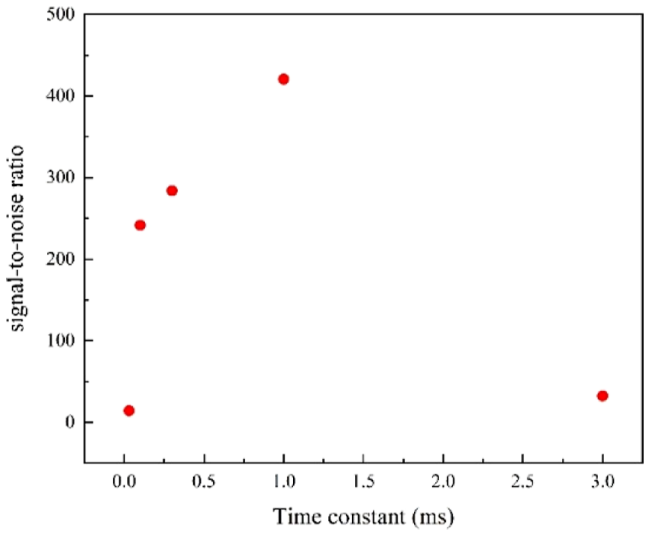

Figure 7. Photoacoustic heterodyne sensor signal-to-noise ratio as a function of the lock-in amplifier time constant.

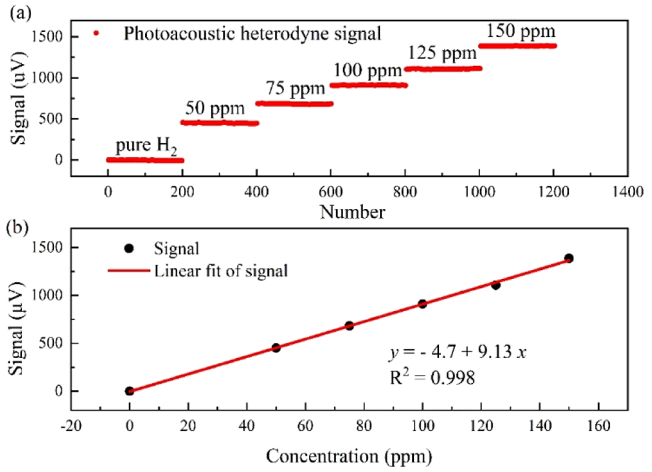

Figure 8. (a) Photoacoustic heterodyne signals from the different concentration levels of CO; (b) linearity of the photoacoustic heterodyne sensor.

0.998 obtained from the linear fit, confirming the sensor's linear response to the carbon monoxide concentration in H_2.

The photoacoustic heterodyne sensor presented in this study exhibits a significantly faster response compared to that of previously reported CO sensors, albeit with a lower detection limit. This level of performance is satisfactory for monitoring CO in fuel cells. The decrease in detection sensitivity can be attributed to the substantial drop in the Q-value of the PAC when H_2 is used as the carrier gas, leading to a higher loss of signal generated by the sensor. A comprehensive comparison of the parameters between the sensors reported in previous studies and the ones discussed in this article is shown in Table 1. The response time of the reported sensors without wavelength locking is basically more than 10 s, whereas the sensor described in this paper has a response time of 15 ms. Sensor response speed is improved by 3 orders of magnitude.

The long-term stability of the photoacoustic heterodyne sensor was assessed through Allen-Werle deviation analysis. In this evaluation, the PAC was filled with pure H_2, and measurements were conducted at room temperature and atmospheric pressure conditions. The time constant of the lock-in amplifier was set to 1 ms, and the resulting analytical plot is depicted in Figure 9. Notably, the minimum detection limit reaches 11 ppb at an optimal integration time of ~1 s.

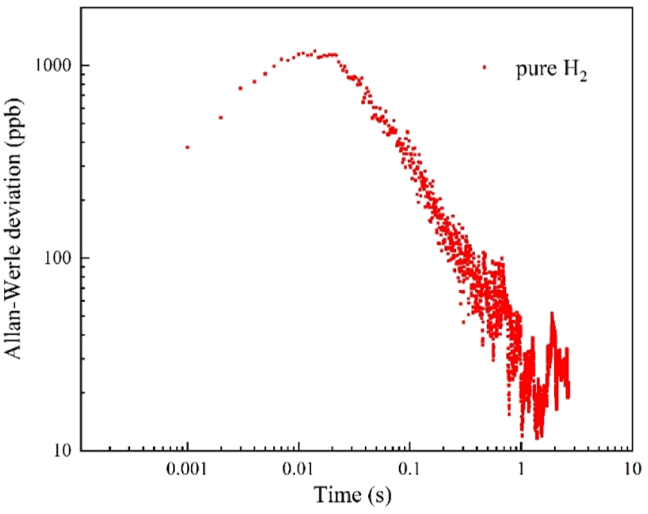

Figure 9. Allan-Werle deviation as a function of the data averaging period measured for pure H_2 samples.

CONCLUSIONS

In this work, a photoacoustic heterodyne sensor is designed for the measurement of the amount of CO in H_2. The sensor utilizes the photoacoustic heterodyne technique and employs a differential PAC as a spectrophone. With an integration time of 1 ms, the sensor achieves a detection limit of 363 ppb, corresponding to an NNEA of 3.76×10^{-8} cm^{-1} W $Hz^{-1/2}$. Compared with the previously reported sensors, the response speed of the sensor has been greatly improved. Furthermore, the sensor's stability was evaluated using the Allan-Werle variance method, revealing that the minimum detection limit can be further improved to 11 ppb by increasing the integration time to 1 s. The developed sensor offers several advantages, including fast response, calibration-free operation,

Table 1. Performance Comparison of the Developed PAH CO Sensor and Previously Reported Techniques

refs	technique	wavelength (μm)	power	time constant (ms)	response time	sensitivity	carrier gas
44	QEPAS	4.61	21 mW	300		7 ppb	N_2
45	PAS	1.56	9.5 W	1000	20 s	110 ppb	SF_6
46	QEPAS	2.33	3.7 mW	1000		4.2 ppm	N_2
47	QEPAS	4.61	20 mW	1000	100 s	90 ppb	SF_6
48	LITES	2.33		200		31.6 ppm	N_2
this paper	PAH	4.61	21 mW	1	15 ms	363 ppb	H_2

https://doi.org/10.1021/acs.analchem.3c04753
Anal. Chem. 2024, 96, 547−553

and the absence of wavelength locking. These characteristics align well with the requirements for trace detection of CO in H_2 for fuel cell applications. As part of future work, enhancing the sensor's response to weak signals could be accomplished by designing a high Q-value photoacoustic cell as a spectrophone. This advancement would contribute to improving the minimum detection limit of the sensor.

AUTHOR INFORMATION

Corresponding Authors

Peichao Zheng − *Chongqing Key Laboratory of Optoelectronic Information Sensing and Transmission Technology, School of Optoelectronic Engineering, Chongqing University of Posts and Telecommunications, Chongqing 400065, China*; Email: zhengpc@cqupt.edu.cn

Lei Dong − *State Key Laboratory of Quantum Optics and Quantum Optics Devices, Institute of Laser Spectroscopy and Collaborative Innovation Center of Extreme Optics, Shanxi University, Taiyuan 030006, China*; orcid.org/0000-0001-7379-3388; Email: donglei@sxu.edu.cn

Authors

Biao Li − *Chongqing Key Laboratory of Optoelectronic Information Sensing and Transmission Technology, School of Optoelectronic Engineering, Chongqing University of Posts and Telecommunications, Chongqing 400065, China*

Hongpeng Wu − *State Key Laboratory of Quantum Optics and Quantum Optics Devices, Institute of Laser Spectroscopy and Collaborative Innovation Center of Extreme Optics, Shanxi University, Taiyuan 030006, China*

Chaofan Feng − *State Key Laboratory of Quantum Optics and Quantum Optics Devices, Institute of Laser Spectroscopy and Collaborative Innovation Center of Extreme Optics, Shanxi University, Taiyuan 030006, China*

Jinmei Wang − *Chongqing Key Laboratory of Optoelectronic Information Sensing and Transmission Technology, School of Optoelectronic Engineering, Chongqing University of Posts and Telecommunications, Chongqing 400065, China*

Suotang Jia − *State Key Laboratory of Quantum Optics and Quantum Optics Devices, Institute of Laser Spectroscopy and Collaborative Innovation Center of Extreme Optics, Shanxi University, Taiyuan 030006, China*

Complete contact information is available at: https://pubs.acs.org/10.1021/acs.analchem.3c04753

Author Contributions

B.L. and H.W. have contributed equally to this work. B.L. performed the experiments. H.W. provided experiment guidance. B.L. and H.W. wrote the manuscript. L.D. and P.C. supported the experiments and contributed to the manuscript. C.F., J.W., and S.J. provided technical guidance. All the authors have given approval for the final version of the manuscript.

Notes

The authors declare no competing financial interest.

ACKNOWLEDGMENTS

This work was supported by National Natural Science Foundation of China (NSFC) (nos. 62122045, 62075119, 62235010, and 62175137); National Key R&D Program of China, code: 2019YFE0118200; The High-end Foreign Expert Program (nos. G2023004005L); The Shanxi Science Fund for Distinguished Young Scholars (20210302121003); and Science and Technology Research Program of Chongqing Municipal Education Commission (KJQN202000640 and KJZD-M202200602).

REFERENCES

(1) Sopian, K.; Wan Daud, W. R. *Renewable Energy* **2006**, *31*, 719−727.
(2) Park, E. D.; Lee, D.; Lee, H. C. *Catal. Today* **2009**, *139*, 280−290.
(3) Zamel, N.; Li, X. P. *Energy Gombust.* **2011**, *37*, 292−329.
(4) Matsuda, Y.; Shimizu, T.; Mitsushima, S. *J. Power Sources* **2016**, *318*, 1−8.
(5) Cheng, X.; Shi, Z.; Glass, N.; Zhang, L.; Zhang, J.; Song, D.; Liu, Z.; Wang, H.; Shen, J. *J. Power Sources* **2007**, *165*, 739−756.
(6) Krumpelt, M.; Krause, T. R.; Carter, J. D.; Kopasz, J. P. *Catal. Today* **2002**, *77*, 3−16.
(7) Faur Ghenciu, A. *Curr. Org. Chem. Current.* **2002**, *6*, 389−399.
(8) Song, C. *Catal. Today* **2002**, *77*, 17−49.
(9) Zhang, J.; Wang, H.; Wilkinson, D. P.; Song, D.; Shen, J.; Liu, Z. S. *J. Power Sources* **2005**, *147*, 58−71.
(10) https://www.iea.org/reports/the-future-of-hydrogen. June, 2019.
(11) Delgado, S.; Lagarteira, T.; Mendes, A. *Int. J. Electrochem. Sci.* **2020**, *15*, 613−627.
(12) Li, Y.; Wang, X.; Mei, B.; Wang, Y.; Luo, Z.; Luo, E.; Yang, X.; Shi, Z.; Liang, L.; Jin, Z.; Wu, Z.; Jiang, Z.; Liu, C.; Xing, W.; Ge, J. *J. Sci. Bull.* **2021**, *66*, 1305−1311.
(13) Garbis, P.; Kern, C.; Jess, A. *Energies* **2019**, *12*, 469.
(14) Peters, R.; Meißner, J. *Chem. Eng. Technol.* **2004**, *76*, 1555−1558.
(15) Ariyaratne, R.; Elangasinghe, M. A.; Zamora, M. L.; Karunaratne, D. G. G. P.; Manipura, A.; Jinadasa, K. B. S. N.; Abayalath, K. H. N. *Sens. Actuators, B* **2023**, *390*, 133935.
(16) Afshar-Mohajer, N.; Zuidema, C.; Sousan, S.; Hallett, L.; Tatum, M.; Rule, A. M.; Thomas, G.; Peters, T. M.; Koehler, K. *J. Occup. Environ. Hyg.* **2018**, *15*, 87−98.
(17) Krivetskiy, V.; Efitorov, A.; Arkhipenko, A.; Vladimirova, S.; Rumyantseva, M.; Dolenko, S.; Gaskov, A. *Sens. Actuators, B* **2018**, *254*, 502−513.
(18) Dey, A. *Mater. Sci. Eng., A* **2018**, *229*, 206−217.
(19) Hosoya, A.; Tamura, S.; Imanaka, N. *ISIJ Int.* **2016**, *56*, 1634−1637.
(20) Bhargav, K. K.; Ram, S.; Labhsetwar, N.; Majumder, S. B. *Sens. Actuators, B* **2015**, *206*, 389−398.
(21) Dong, L.; Kosterev, A. A.; Thomazy, D.; Tittel, F. K. *Appl. Phys. B: Lasers Opt.* **2010**, *100*, 627−635.
(22) Kosterev, A. A.; Bakhirkin, Y. A.; Curl, R. F.; Tittel, F. K. *Opt. Lett.* **2002**, *27*, 1902−1904.
(23) Wei, T.; Zifarelli, A.; Dello Russo, S.; Wu, H.; Menduni, G.; Patimisco, P.; Sampaolo, A.; Spagnolo, V.; Dong, L. *Appl. Phys. Rev.* **2021**, *8*, 041409.
(24) Hu, M.; Ventura, A.; Hayashi, J. G.; Poletti, F.; Yao, S.; Ren, W.; Ren, W. *Sens. Actuators, B* **2022**, *363*, 131774.
(25) Lin, H.; Zheng, H.; Montano, B. A. Z.; Wu, H.; Giglio, M.; Sampaolo, A.; Patimisco, P.; Zhu, W.; Zhong, Y.; Dong, L.; Kan, R.; Yu, J.; Spagnolo, V. *Photoacoustics* **2022**, *25*, 100321.
(26) Liu, K.; Mei, J.; Zhang, W.; Chen, W.; Gao, X. *Sens. Actuators, B* **2017**, *251*, 632−636.
(27) Liu, K.; Lewicki, R.; Tittel, F. K. *Sens. Actuators, B* **2016**, *237*, 887−893.
(28) Ma, Y.; Hu, Y.; Qiao, S.; Lang, Z.; Liu, X.; He, Y.; Spagnolo, V. *Photoacoustics* **2022**, *25*, 100329.
(29) Ma, Y.; Hong, Y.; Qiao, S.; Lang, Z.; Liu, X. *Opt. Lett.* **2022**, *47*, 601−604.
(30) Yin, X.; Dong, L.; Wu, H.; Gao, M.; Zhang, L.; Zhang, X.; Liu, L.; Shao, X.; Tittel, F. K. *Photoacoustics* **2022**, *25*, 100319.

(31) Borri, S.; Patimisco, P.; Sampaolo, A.; Beere, H. E.; Ritchie, D. A.; Vitiello, M. S.; Scamarcio, G.; Spagnolo, V. *Appl. Phys. Lett.* **2013**, *103*, 021105.
(32) Chen, K.; Zhang, B.; Guo, M.; Chen, Y.; Deng, H.; Yang, B.; Liu, S.; Ma, F.; Zhu, F.; Gong, Z.; Yu, Q. *Sens. Actuators, B* **2020**, *310*, 127825.
(33) Chen, K.; Yu, Q.; Gong, Z.; Guo, M.; Qu, C. *Sens. Actuators, B* **2018**, *268*, 205−209.
(34) Spagnolo, V.; Patimisco, P.; Borri, S.; Scamarcio, G.; Bernacki, B. E.; Kriesel, J. *Opt. Lett.* **2012**, *37*, 4461−4463.
(35) Patimisco, P.; Sampaolo, A.; Dong, L.; Tittel, F. K.; Spagnolo, V. *Appl. Phys. Rev.* **2018**, *5*, 011106.
(36) Sigrist, M. W. *J. Adv. Res.* **2015**, *6*, 529−533.
(37) Yin, X.; Su, Y.; Xi, T.; Chen, B.; Zhang, L.; Zhang, X.; Liu, L.; Shao, X. *J. Appl. Phys.* **2022**, *131*, 130701.
(38) Zheng, K.; Zheng, C.; Ma, N.; Liu, Z.; Yang, Y.; Zhang, Y.; Wang, Y.; Tittel, F. K. *ACS Sens.* **2019**, *4*, 1899−1908.
(39) Shang, Z.; Li, S.; Li, B.; Wu, H.; Sampaolo, A.; Patimisco, P.; Spagnolo, V.; Dong, L. *Photoacoustics* **2022**, *26*, 100363.
(40) Wu, H.; Dong, L.; Zheng, H.; Yu, Y.; Ma, W.; Zhang, L.; Yin, W.; Xiao, L.; Jia, S.; Tittel, F. K. *Nat. Commun.* **2017**, *8*, 15331.
(41) Li, B.; Feng, C.; Wu, H.; Jia, S.; Dong, L. *Sens. Actuators, B* **2022**, *358*, 131510.
(42) Yin, X.; Wu, H.; Dong, L.; Li, B.; Ma, W.; Zhang, L.; Yin, W.; Xiao, L.; Jia, S.; Tittel, F. K. *ACS Sens.* **2020**, *5*, 549−556.
(43) Li, B.; Feng, C.; Wu, H.; Jia, S.; Dong, L. *Photoacoustics* **2022**, *27*, 100388.
(44) Li, S.; Dong, L.; Wu, H.; Sampaolo, A.; Patimisco, P.; Spagnolo, V.; Tittel, K. *Anal. Chem.* **2019**, *91*, 5834−5840.
(45) Yin, X.; Wu, H.; Dong, L.; Ma, W.; Zhang, L.; Yin, W.; Xiao, L.; Jia, S.; Tittel, F. K. *Sens. Actuators, B* **2019**, *282*, 567−573.
(46) Ma, Y.; Tong, Y.; He, Y.; Jin, X.; Tittel, F. K. *Opt. Express* **2019**, *27*, 9302−9312.
(47) Sun, B.; Zifarelli, A.; Wu, H.; Dello Russo, S.; Li, S.; Patimisco, P.; Dong, L.; Spagnolo, V. *Anal. Chem.* **2020**, *92*, 13922−13929.
(48) Chen, W.; Qiao, S.; He, Y.; Jiang, J.; Shi, Y.; Ma, Y. *Infrared Phys. Technol.* **2023**, *135*, 104938.

https://doi.org/10.1021/acs.analchem.3c04753
Anal. Chem. 2024, 96, 547−553